The high-resolution crystal structure of phosphatidylinositol 4-kinase IIβ and the crystal structure of phosphatidylinositol 4-kinase IIα containing a nucleoside analogue provide a structural basis for isoform-specific inhibitor design

Martin Klima, Adriana Baumlova, Dominika Chalupska, Hubert Hřebabecký, Milan Dejmek, Radim Nencka and Evzen Boura*

Department of Biochemistry, Institute of Organic Chemistry and Biochemistry, Flemingovo nam. 2, 166 10 Prague, Czech Republic. *Correspondence e-mail: boura@uochb.cas.cz

Phosphatidylinositol 4-phosphate (PI4P) is the most abundant monophospho-inositide in eukaryotic cells. Humans have four phosphatidylinositol 4-kinases (PI4Ks) that synthesize PI4P, among which are PI4K IIβ and PI4K IIα. In this study, two crystal structures are presented: the structure of human PI4K IIβ and the structure of PI4K IIα containing a nucleoside analogue. The former, a complex with ATP, is the first high-resolution (1.9 Å) structure of a PI4K. These structures reveal new details such as high conformational heterogeneity of the lateral hydrophobic pocket of the C-lobe and together provide a structural basis for isoform-specific inhibitor design.

1. Introduction

Phosphatidylinositol 4-phosphate (PI4P) is the most abundant monophosphoinositide in the eukaryotic cell. PI4P, together with other phosphoinositides (PIPs), regulates many cellular processes, including vesicle trafficking, cell signalling, auto-phagy and cell survival, and has been implicated in the pathogenesis of many human diseases (Balla, 2013; Tan & Brill, 2014; Wang *et al.*, 2012; Waugh, 2015). Furthermore, PI4P is a key lipid marker of the Golgi and TGN, plays an important role in cell signalling and serves as a precursor for polyphosphoinositides (Balla, 2013; Tan & Brill, 2014). Humans have four phosphatidylinositol 4-kinases (PI4Ks) that synthesize PI4P. The type III PI4Ks (PI4K IIIα and PI4K IIIβ) are soluble cytoplasmic proteins that share homology with PI3Ks and are recruited to membranes transiently *via* protein–protein interactions (Wu *et al.*, 2014; Sasaki *et al.*, 2012; Greninger *et al.*, 2012). Conversely, the type II PI4Ks (PI4K IIα and PI4K IIβ) are active only when palmitoylated and anchored in the membrane. PI4K IIα is the most active PI4K and is almost exclusively localized to membranes as a consequence of its palmitoylation (Barylko *et al.*, 2001). PI4K IIβ is localized in the cytoplasm, where it is stabilized by the Hsp90 chaperone (Jung *et al.*, 2011) and translocates to the plasma membrane in response to activated Rac (Balla *et al.*, 2002; Wei *et al.*, 2002). Both type II and type III PI4Ks are important players in vesicular trafficking (Jović *et al.*, 2012; Burgess *et al.*, 2012). They contribute to the recruitment of the clathrin adaptor complexes AP1 and AP3 (Craige *et al.*, 2008), regulate the endosomal sorting of VAMP3 (Jović *et al.*, 2014) and are
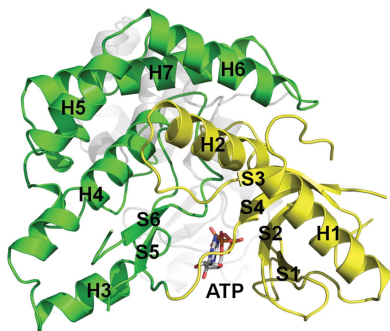
important for EGF receptor targeting to the lysosome (Minogue *et al.*, 2006).

Recent crystal structures of PI4K IIα and PI4K IIIβ (Baumlova *et al.*, 2014; Zhou *et al.*, 2014; Burke *et al.*, 2014) have emphasized the structural similarity of the type III PI4Ks to other lipid kinases such as PI3Ks and revealed that the type II enzymes are rather more similar to protein Ser/Thr kinases [for example, the cell translocating kinase A (CtkA) from *Helicobacter pylori*; Kim *et al.*, 2010]. Type III PI4Ks have recently been identified as essential host factors for the replication of single-strand positive-sense RNA (+RNA) viruses (Berger *et al.*, 2009; Altan-Bonnet & Balla, 2012). Type II PI4Ks, on the other hand, are exploited by intracellular bacteria such as *Legionella pneumophila* and *Chlamydia trachomatis* (Moorhead *et al.*, 2010; Weber *et al.*, 2006) and play a role in the Wnt signalling pathway (Qin *et al.*, 2009), a pathway that is often upregulated in cancer. As a result, PI4Ks are considered to be a pharmacological target. Potent and isoform-selective inhibitors would be a great tool to further dissect the biological role of each PI4K family member and, in addition, would be potentially useful in human medicine. Unfortunately, no specific inhibitors of type II PI4Ks are yet available. High-resolution crystal structures are very useful tools for inhibitor design. The previously solved structures of PI4Ks (PI4K IIα and PI4K IIIβ) have been obtained in the resolution range 2.8–3.3 Å and PI4K IIα has only been crystallized with ATP or ADP. Here, we present the crystal structure of PI4K IIβ solved at 1.9 Å resolution (the first high-resolution structure of a PI4K) and the structure of PI4K IIα containing a bound nucleoside analogue. The structures reveal details of ATP binding, show the conformation heterogeneity of the allosteric hydrophobic pocket and provide a structural basis for nucleoside scaffold-based inhibitor design.

2. Materials and methods

2.1. Protein expression and purification

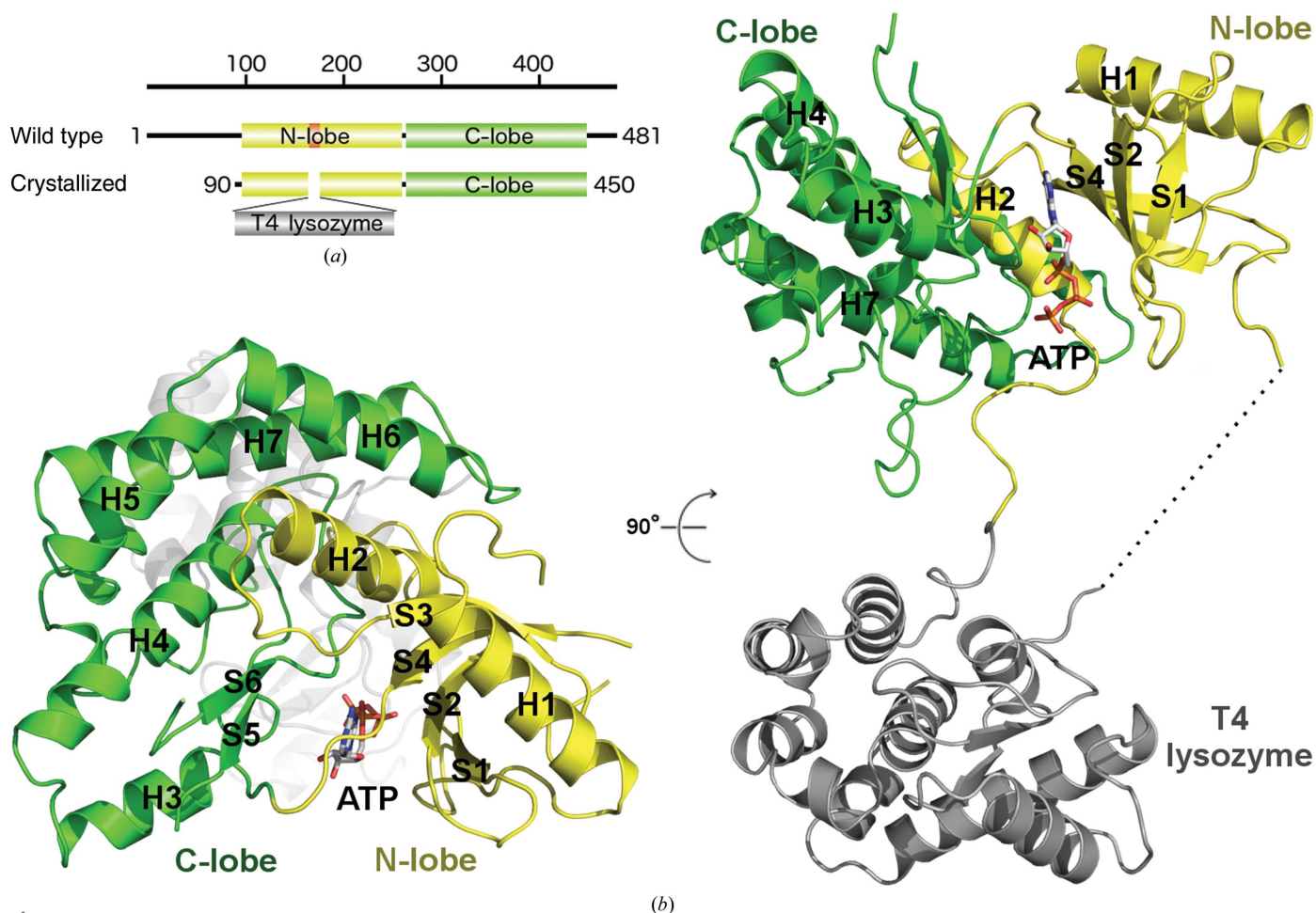Pseudo wild-type (pseudo-wt) PI4K IIα (UniProt code Q9BTU6) and the crystallographic construct were expressed

Figure 1
The overall fold of PI4K IIβ. (*a*) Schematic representation of wild-type PI4K IIβ and the chimeric construct used for crystallization. The N-lobe and C-lobe of PI4K IIβ are shown in yellow and green, respectively; the palmitoylated cysteine-rich motif of PI4K IIβ is shown in orange and the T4 lysozyme in grey. (*b*) Overall fold of PI4K IIβ. The protein backbone is shown as a cartoon representation. The N-lobe is depicted in yellow, the C-lobe in green and the T4 lysozyme in grey. In the left panel, the front view is shown, in which the N-lobe, the C-lobe and the ATP-binding groove in between are emphasized; in the right panel, the view is rotated by 90° to place the T4 lysozyme at the bottom. The kinase is composed of seven α-helices numbered H1–H7 and six β-sheets numbered S1–S6.

Table 1
Data collection and processing.

Values in parentheses are for the outer shell.

Crystal	PI4K IIβ	PI4K IIα + MD59
Diffraction source	MX14.1 beamline, BESSY II	MX14.1 beamline, BESSY II
Wavelength (Å)	1.28272	0.918409
Temperature (K)	100	100
Detector	Pilatus 6M	Pilatus 6M
Crystal-to-detector distance (mm)	375.7	647.3
Rotation range per image (°)	0.2	0.1
Total rotation range (°)	240	110
Exposure time per image (s)	0.8	0.5
Space group	$P4_12_12$	$P2_12_12$
Unit-cell parameters (Å, °)	$a = 106.01$, $b = 106.01$, $c = 214.53$, $\alpha = \beta = \gamma = 90$	$a = 79.41$, $b = 103.77$, $c = 78.11$, $\alpha = \beta = \gamma = 90$
Resolution range (Å)	47.52–1.90 (1.97–1.90)	49.07–2.58 (2.67–2.58)
Total No. of reflections	1704172 (165811)	75199 (4056)
No. of unique reflections	96773 (9513)	20124 (1535)
Completeness (%)	99.98 (99.94)	95.77 (74.15)
Multiplicity	17.6 (17.4)	3.7 (2.6)
$\langle I/\sigma(I) \rangle$	17.40 (1.95†)	15.98 (2.36)
$R_{r.i.m.}$‡ (%)	10.5 (156.2)	7.14 (40.4)
Overall B factor from Wilson plot (Å²)	36.26	43.95

† It has been shown that including data with mean $I/\sigma(I) < 2.0$ leads to improved maps (Karplus & Diederichs, 2012). The *XDSAPP* program (Krug *et al.*, 2012) suggested a 1.83 Å resolution cutoff. We decided to be more conservative and cut the data at 1.9 Å resolution, leading to $I/\sigma(I) = 1.95$ in the highest resolution shell. Please note that $I/\sigma(I) = 2$ at 1.94 Å resolution. ‡ The $R_{r.i.m.}$ value was estimated by multiplying the conventional R_{merge} value by the factor $[N/(N − 1)]^{1/2}$, where N is the data multiplicity.

and purified as described previously (Baumlova *et al.*, 2014) as was the PI4K IIIβ (Burke *et al.*, 2014). The gene for full-length PI4K IIβ (amino-acid sequence 1–481; UniProt code Q8TCG2) does not significantly express in bacteria. Therefore, we omitted the N-terminal part that is predicted to be disordered and is not important for the catalytic activity of the kinase (Jung *et al.*, 2008). PI4K IIβ 90–481 was cloned into the first cassette of the pRSFD vector (Novagen) with an N-terminal 6×His tag followed by the GB1 solubility tag and the TEV protease-cleavage site. However, our attempts to express this construct of PI4K IIβ produced only low yields that were contaminated with Hsp70 and Hsp90 chaperones which were difficult to remove, suggesting that the protein had folding complications. As a result, we employed the same strategy that produced well diffracting crystals of the PI4K IIα enzyme: we truncated the C-terminus, which is flexible and thus impedes crystallization (Różycki & Boura, 2014), and we inserted T4 lysozyme instead of the cysteine-rich motif 169-VCCPCCF-175 of PI4K IIβ that corresponds to the 173-LCCPCCF-179 motif of the PI4K IIα enzyme. The resulting construct PI4K IIβ 90–450 with a T4 insertion was expressed at high levels and could be purified to homogeneity (see below) but did not crystallize. Therefore, we had to screen the T4 insertion boundaries. All constructs with changed boundaries were expressed, but only the construct in which the sequence 166-VHKVCCPCCF-175 was replaced by T4 lysozyme (Fig. 1*a*) produced diffraction-quality crystals.

The cysteine-rich loop 166-VHKVCCPCCF-175 was replaced by T4 lysozyme using the QuikChange kit (Strata-

Table 2
Structure solution and refinement.

Values in parentheses are for the outer shell.

Crystal	PI4K IIβ	PI4K IIα + MD59
Resolution range (Å)	47.52–1.90 (1.97–1.90)	49.07–2.58 (2.67–2.58)
Completeness (%)	99.98 (99.94)	95.77 (74.15)
No. of reflections, working set	91934	19117
No. of reflections, test set	4839	1007
Final R_{work} (%)	21.01 (28.60)	21.52 (29.58)
Final R_{free} (%)	24.20 (33.16)	25.48 (42.87)
No. of non-H atoms		
Total	7387	3943
Protein	7011	3882
Ligand	62	46
Water	277	3
R.m.s. deviations		
Bonds (Å)	0.009	0.012
Angles (°)	1.04	1.63
Average B factors (Å²)		
Protein	41.80	60.10
Ligands	43.60	67.33
Solvent	39.40	61.50
Ramachandran plot		
Most favoured (%)	97	96
Outliers (%)	0	0

gene). The protein was purified using an affinity and size-exclusion chromatography procedure previously developed in our laboratory (Nemecek *et al.*, 2013; Boura *et al.*, 2010). Briefly, the protein was expressed in *Escherichia coli* BL21 Star cells. The bacterial cells were lysed in lysis buffer [50 m*M* Tris pH 8, 300 m*M* NaCl, 3 m*M* β-mercaptoethanol (β-ME), 40 m*M* imidazole, 10% glycerol] and the lysate was incubated with Ni–NTA resin (Macherey–Nagel) and extensively washed with lysis buffer. The protein was eluted with lysis buffer supplemented with imidazole (300 m*M*). The tags were removed with TEV protease and the protein was further purified using size-exclusion chromatography with a Superdex 200 column (GE Healthcare) in SEC buffer (10 m*M* MES pH 6.5, 200 m*M* NaCl, 3 m*M* β-ME). Proteins were concentrated to 5.4 mg ml⁻¹ and stored at −80°C. The protein concentration was estimated using theoretical extinction coefficients (90 300 for PI4K IIα with a T4 insertion and 88 190 for PI4K IIβ with a T4 insertion) calculated using the *PROTEIN CALCULATOR* web server (http://protcalc.sourceforge.net/).

2.2. Crystallization and crystallographic analysis

For the crystallization trials, the PI4K IIβ 90–450 enzyme with a T4 insertion was supplemented with ATP (5 m*M*) and MgCl₂ (2 m*M*). Crystals grew in 2 d at 291 K in a sitting drop consisting of a 1:1 mixture of the protein solution and well solution [100 m*M* MES–imidazole pH 6.5, 10%(*w/v*) PEG 4000, 20%(*v/v*) glycerol, 20 m*M* 1,6-hexanediol, 20 m*M* 1-butanol, 20 m*M* 1,2-propanediol, 20 m*M* 2-propanol, 20 m*M* 1,4-butanediol, 20 m*M* 1,3-propanediol] as summarized in Supplementary Table S1. The crystals were flash-cooled in liquid nitrogen and analysed on the MX14.1 beamline at BESSY II using a Pilatus 6M detector. They diffracted to 1.9 Å resolution and belonged to the tetragonal space group $P4_12_12$.

For the crystallization trials with the MD59 nucleoside analogue, the PI4K IIα enzyme with a T4 insertion was supplemented with MD59 (2 m*M*) and ADP (0.5 m*M*). Crystals grew in 2 d at 291 K in a sitting drop consisting of a 1:1 mixture of protein solution and well solution [100 m*M* HEPES pH 7.0, 10%(*w/v*) PEG 4000, 10%(*v/v*) 2-propanol] as summarized in Supplementary Table S1. The crystals were cryoprotected in well solution supplemented with 20%(*v/v*) glycerol and flash-cooled in liquid nitrogen. They diffracted to 2.6 Å resolution and belonged to space group $P2_12_12$.

The crystallographic data sets were collected from single cooled crystals. Data were integrated and scaled using *XDS* (Kabsch, 2010); the data quality is summarized in Table 1. The structure was solved by molecular replacement (MR) using *Phaser* (McCoy *et al.*, 2007) from the *CCP*4 package (Winn *et al.*, 2011). The structure of PI4K IIα with a T4 insertion (PDB entry 4pla; Baumlova *et al.*, 2014) was used as a search model. The ligands were placed using *Coot* (Debreczeni & Emsley, 2012) and the structures were refined in *PHENIX* (*xyz* coordinates, real-space and rotamers but no TLS or NCS; Adams *et al.*, 2010) as summarized in Table 2. Structural figures were generated in *PyMOL* (Schrödinger). The atomic coordinates were deposited in the Protein Data Bank (http://www.pdb.org)

under accession codes 4wtv for PI4K IIβ and 4yc4 for PI4K IIα complexed with MD59.

2.3. *In vitro* kinase assay

In vitro kinase activity was measured using a standard procedure (Tai *et al.*, 2011). Briefly, reactions were carried out in a total volume of 5 µl in a 384-well plate format by mixing three stock solutions: 1 µl of the pseudo-wt PI4K IIα (the T4 insertion renders the enzyme inactive) or PI4K IIIβ enzyme (final concentration 100 n*M*) in kinase buffer (20 m*M* Tris pH 7.5, 5 m*M* MgCl$_2$, 0.2% Triton X-100, 0.1 mg ml^{-1} BSA, 2 m*M* DTT), 1 µl of PI in kinase buffer (50 µ*M* final concentration) and 1 µl of the small molecule at the desired concentration. The reaction was started by adding 2 µl of ATP in kinase buffer (final concentration 100 µ*M*). The reaction was carried out for 60 min at room temperature (295 K) and the amount of hydrolyzed ATP was measured according to the manufacturer's protocol (5 µl of ADP/Glo™ Reagent was added to terminate the kinase reaction and deplete the remaining ATP, and 10 µl of Kinase Detection Reagent was then added to simultaneously convert ADP to ATP and to allow the newly synthesized ATP to be measured by the luciferase/luciferin
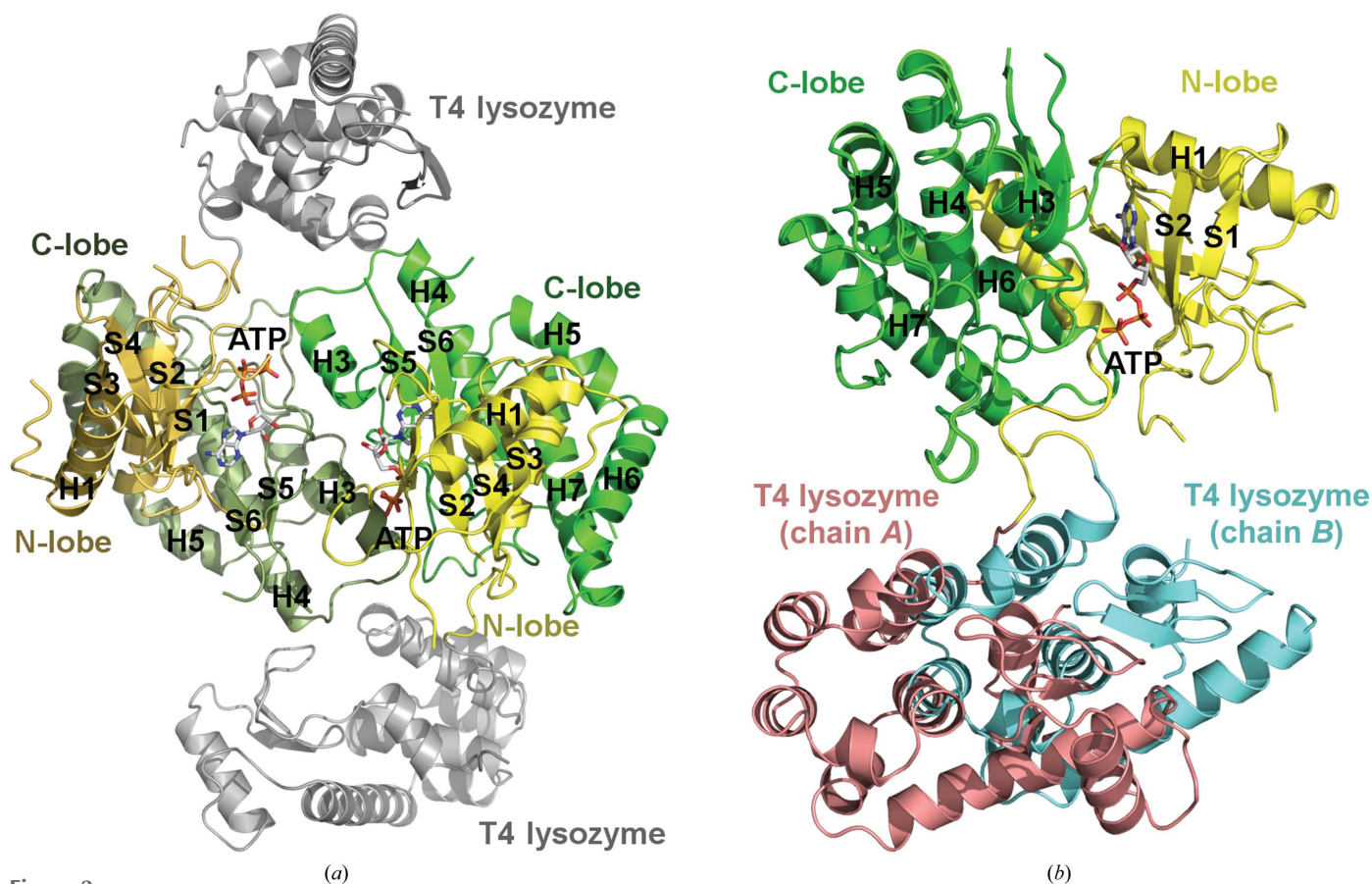

Figure 2
The asymmetric unit content. (*a*) The crystals contained two molecules of PI4K IIβ per asymmetric unit. The N-lobe and C-lobe of PI4K IIβ are shown in yellow and green, respectively. The T4 lysozyme is shown in grey. The second molecule is coloured in the same way except that darker tones are used. (*b*) Superposition of chain *A* and chain *B* according to the kinase domain of the chimeric PI4K IIβ/T4 construct reveals that the two copies of T4 lysozyme in the asymmetric unit are differently tilted with respect to the kinase domain. The N-lobe and C-lobe of PI4K IIβ are shown in yellow and green, respectively. The T4 lysozyme from chain *A* and chain *B* is shown in salmon and cyan, respectively.

reaction). Luminiscence was measured using a Tecan Infinite M 1000 plate reader.

2.4. Chemical synthesis of the inhibitors MD59 and AdeN3

Compounds MD59 and AdeN3 were prepared according to previously reported procedures (Dejmek *et al.*, 2015; Anglin *et al.*, 2012) as detailed in the Supporting Information.

3. Results and discussion

3.1. The structure of PI4K IIβ

The overall fold of PI4K IIβ (Fig. 1b) is highly similar to the fold of PI4K IIα (they superpose with an r.m.s.d. of 1.12 Å; see Supplementary Fig. S1), which would be expected given the primary-sequence similarity: the major differences are localized to the disordered N-termini, which were not included in the crystallized construct, whereas the kinase domain is conserved (Supplementary Fig. S2). The kinase domain can be divided into N-terminal and C-terminal lobes. The N-lobe of PI4K IIβ consists of two α-helices (H1–H2) surrounding four small antiparallel β-sheets (S1–S4). The C-lobe consists of two α-helices (H3–H4) surrounding two antiparallel β-sheets (S5–S6) located proximally to the ATP-binding groove, and another three α-helices (H5–H6) located more distally and forming a scaffold for the catalytically active part of the kinase and/or providing its allosteric regulation. The catalytic site with ATP bound is localized between the lobes and is formed

mainly by both stretches of antiparallel β-sheets mentioned above and their neighbourhood. The asymmetric unit contained two molecules of PI4K IIβ (Fig. 2a). Interestingly, they contained differently tilted T4 lysozymes (Fig. 2b), probably owing to crystal contacts, yet the conformation of the enzyme remained the same. This fact further supports the current evidence that the insertion of T4 lysozyme instead of a disordered loop does not influence the conformation of the molecule with the insertion (Zou *et al.*, 2012; Rosenbaum *et al.*, 2007).

3.2. Conformational heterogeneity of the lateral hydrophobic pocket

A lateral hydrophobic pocket important for the activity of the PI4K IIα enzyme was identified during structural analysis (Baumlova *et al.*, 2014; Zhou *et al.*, 2014). Comparison of the hydrophobic pocket conformation of PI4K IIβ with both previously published structures of PI4K IIα (Fig. 3) reveals its high conformational heterogeneity, especially of tryptophan residues Trp366 and Trp357. While the observed conformations may be affected by crystal packing, they still confirm the flexibility of this pocket. These findings structurally support its hypothesized function: to promiscuously bind hydrophobic ligands present within the lipid bilayer. Notably, the surface-exposed hydrophobic side chain of residue Trp357 (corresponding to Trp359 in PI4K IIα) is not resolved in our structure, highlighting its flexibility. Surface-exposed hydrophobic
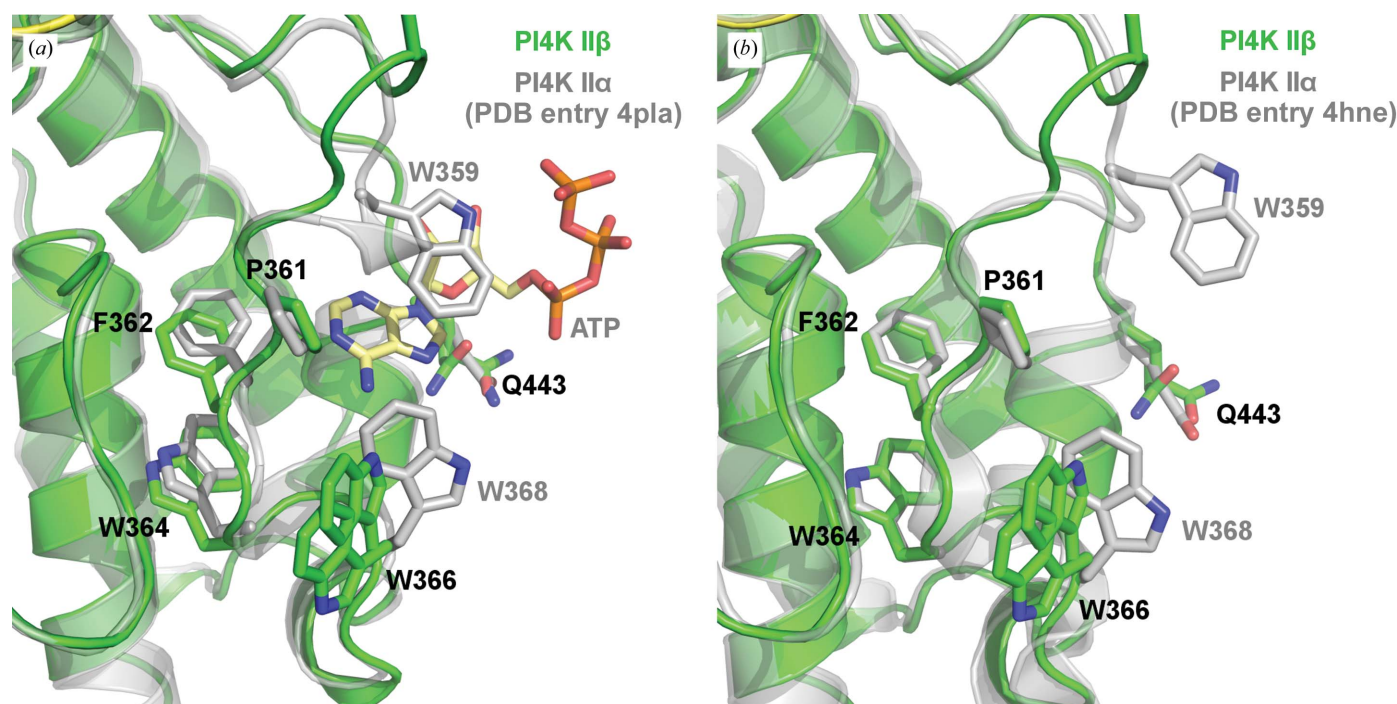

Figure 3
Comparison of the lateral hydrophobic pockets of PI4K IIα and PI4K IIβ. (*a*) Detailed view of the lateral hydrophobic pocket of PI4K IIα (PDB entry 4pla) superposed with the corresponding region of PI4K IIβ. The protein backbone is shown in cartoon representation, the C-lobe of PI4K IIα is coloured grey and the C-lobe of PI4K IIβ is coloured green. ATP bound to PI4K IIα and the side chains of selected residues are shown in stick representation and coloured according to element: oxygen, red; nitrogen, blue; phosphorus, orange. Kinase C atoms are coloured according to their domain assignment and the ATP C atoms are shown in light yellow. H atoms are not shown. (*b*) Detailed view of the lateral hydrophobic pocket of PI4K IIα (PDB entry 4hne; Zhou *et al.*, 2014) superposed with the corresponding region of PI4K IIβ in the same representation and coloured as in (*a*).

residues are rare in proteins, and in the case of membrane-binding proteins they often serve as anchors to the membrane (Boura & Hurley, 2012; Boura *et al.*, 2012) and are one possible method by which proteins can induce membrane curvature (Hurley *et al.*, 2010; Różycki *et al.*, 2012). We thus propose that Trp357 is such an anchor. This is supported by the fact that when the corresponding residue in PI4K IIα is mutated the catalytic activity is impaired (Baumlova *et al.*, 2014) and by the blue shift of the internal tryptophan residues upon liposome binding observed in the case of the PI4K IIα enzyme (Zhou *et al.*, 2014).

3.3. The catalytic site of PI4K IIβ and its comparison with previous PI4K structures

One of the main goals of this study was to obtain detailed structural information about the catalytic site for the future design of inhibitors specific for type II PI4Ks. Owing to the high resolution that we obtained, we were able to precisely model the ATP in the catalytic site (Fig. 4). The ATP is held in place by a complex network of hydrogen bonds to residues of both the N-lobe and C-lobe, as summarized in Fig. 4(*a*). ATP was observed in two alternative conformations that mainly differ in the position of the β-phosphate, which forms hydrogen bonds to Ser133 only in the major conformation (occupancies of 72 and 54% for the two molecules in the asymmetric unit); these hydrogen bonds are absent in the alternative conformation.

3.4. Towards nucleoside-based inhibitors specific for type II PI4Ks

Specific inhibitors of type III PI4Ks have been described (Bianco *et al.*, 2012; van der Schaar *et al.*, 2013; Mejdrova *et al.*, 2015), but no inhibitors of type II enzymes have been reported. This represents a major shortcoming, as such inhibitors would be a good tool to elucidate the function of type II enzymes in cell cultures. In addition, both PI4K IIβ and PI4K IIα are part of the Wnt signalling pathway, a pathway that is often upregulated in cancer, and PI4K IIα is exploited by several intracellular bacteria; therefore, specific inhibitors would have medical importance.

It has been known for decades that type II but not type III PI4Ks are inhibited by adenosine and calcium (Balla, 1998), suggesting that an adenosine scaffold would be an appropriate starting point for type II-specific inhibitor design. Thus, we decided to screen our series of adenosine analogues for their inhibitory activities. We found that compound MD59 (Fig. 5a) exhibited moderate inhibitory activity against type II PI4Ks comparable to but better than that of adenosine and other adenosine-based compounds but had no significant activity against the typical type III PI4Ks (Fig. 5b). These results suggest that inhibitors that share nucleoside-based scaffolds
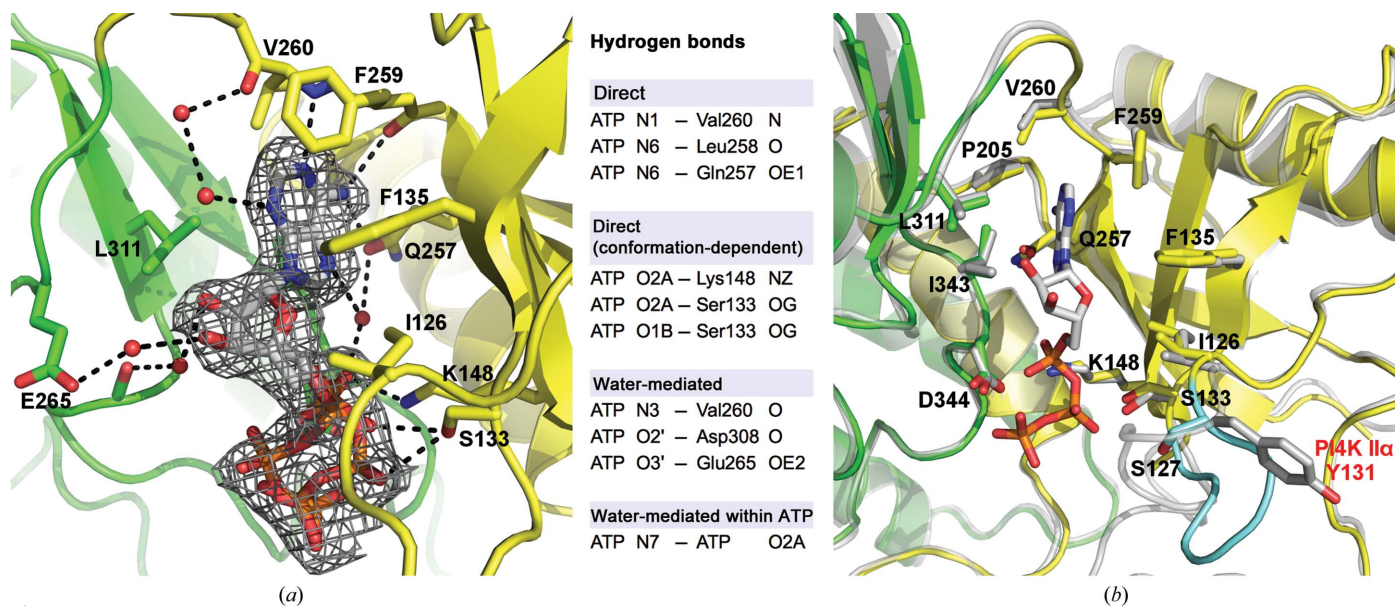

Figure 4
The catalytic site. (*a*) Detailed view of the ATP-binding pocket. The protein backbone is shown in cartoon representation; the N-lobe is coloured yellow and the C-lobe is coloured green. ATP and side chains of selected residues are shown in stick representation and coloured according to element: oxygen, red; nitrogen, blue; phosphorus, orange. The kinase C atoms are coloured according to their domain assignment and the ATP C atoms are shown in silver. Four water molecules are shown as spheres; H atoms are not shown. The unbiased $F_o - F_c$ map contoured at 3σ is shown around the ATP molecule. Hydrogen bonds between ATP, the amino-acid residues and selected water molecules are shown as dotted black lines. Two alternative conformations of the triphosphate moieties of ATP are presented. (*b*) Comparison of the ATP-binding pockets of PI4K IIα and PI4K IIβ. The protein backbone is shown in cartoon representation; PI4K IIα is coloured grey, the N-lobe of PI4K IIβ is coloured yellow and the C-lobe of PI4K IIβ is coloured green. ATP bound to PI4K IIβ and the side chains of selected residues are shown in stick representation and are coloured according to element: oxygen, red; nitrogen, blue; phosphorus, orange. The kinase C atoms are colored according to their domain assignment and ATP C atoms are shown in silver. H atoms are not shown. The poorly ordered loop Ser127–Gly132 of PI4K IIβ is coloured cyan and the PI4K IIα Tyr131 with a different orientation compared with the homologous PI4K IIβ Ser127 is highlighted in red.

also share the same mechanism of action and are capable of inhibiting the atypical type II PI4Ks but not the typical type III PI4Ks (Fig. 5b).

To obtain detailed insight into the function of MD59, we sought to solve the crystal structure of MD59 bound to a type II PI4K. We tried both the PI4K IIα and PI4K IIβ isoforms and succeeded in obtaining crystals with the PI4K IIα isoform. Initially, the crystals diffracted poorly; we hypothesized that the poor diffraction is owing to a missing ligand in the lateral pocket of the C-lobe. Previously, we have shown that a
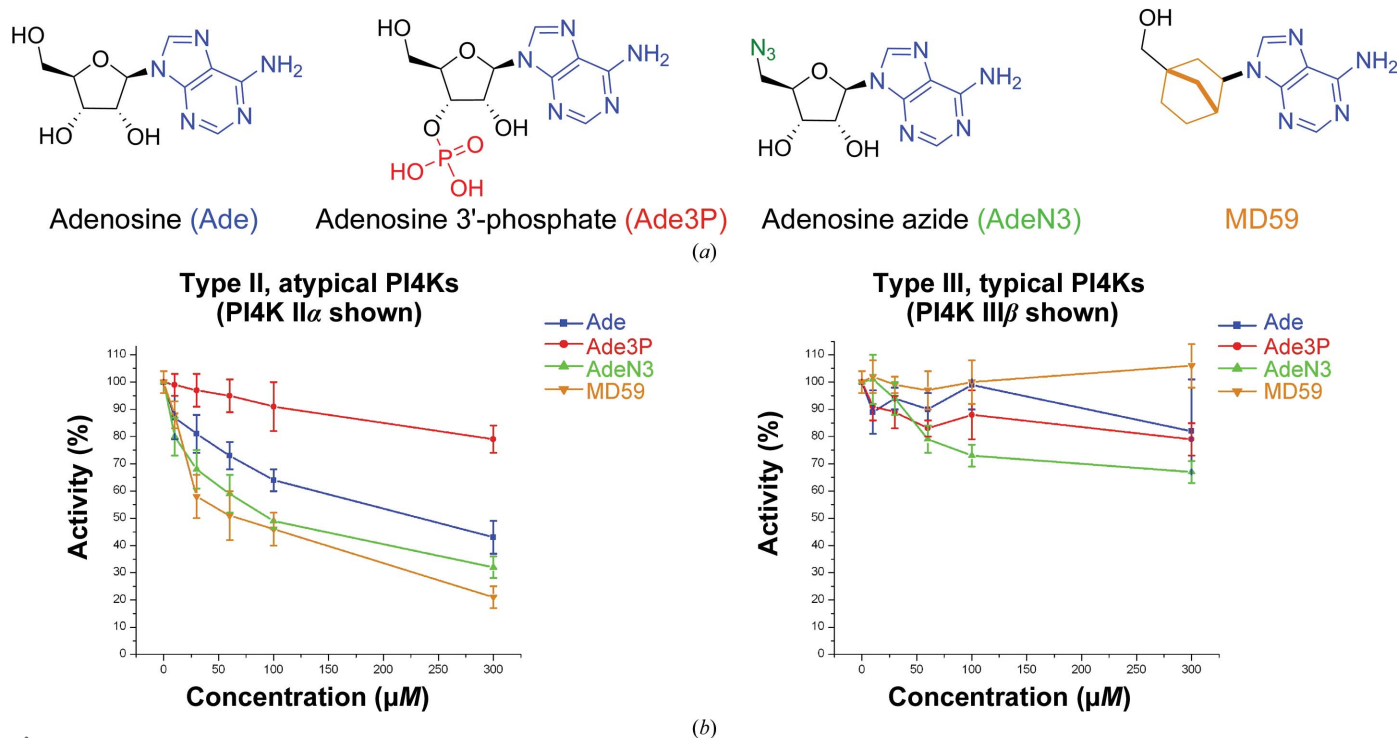

Figure 5
Inhibition of PI4Ks by selected nucleosides and their analogues. (a) Chemical formulae of the nucleosides and analogues used. (b) Inhibitory activity of selected nucleosides and analogues against type II and type III PI4Ks.
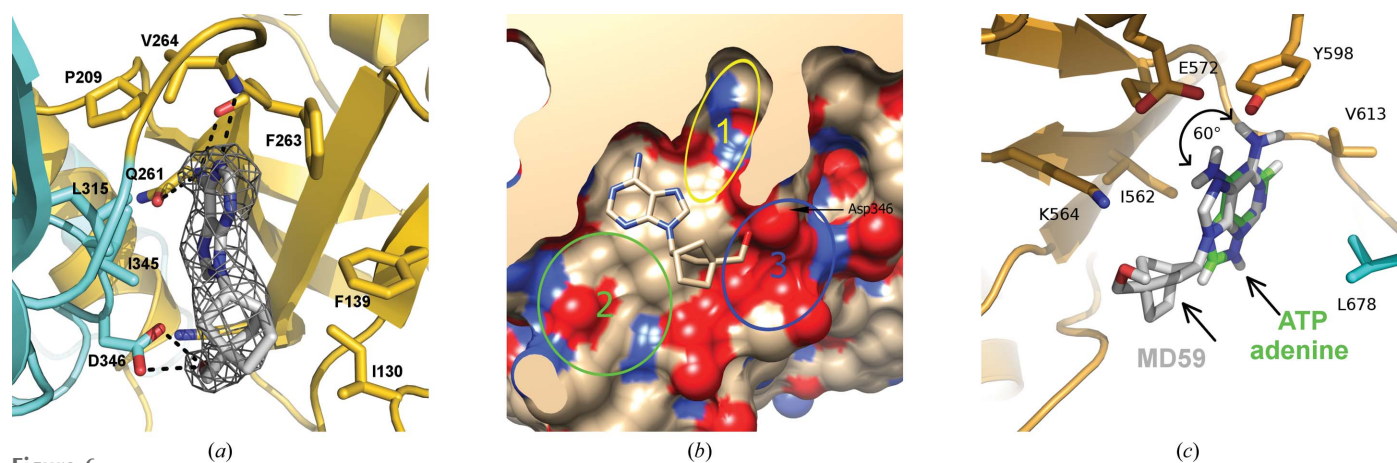

Figure 6
Inhibition of PI4Ks by MD59. (a) Detailed view of the MD59 inhibitor bound in the ATP-binding pocket of PI4K IIα. The protein backbone is shown in cartoon representation; the N-lobe is coloured aquamarine and the C-lobe is coloured gold. MD59 and the side chains of selected residues are shown in stick representation and coloured according to element: oxygen, red; nitrogen, blue. Kinase C atoms are coloured according to domain assignment and the C atoms of MD59 are shown in silver. H atoms are not shown. The unbiased $F_o - F_c$ map contoured at 3σ is shown around the MD59 molecule. Hydrogen bonds between MD59 and the amino-acid residues are shown as dotted black lines. (b) Exploitable pockets in the vicinity of MD59. Design strategies for novel PI4K inhibitors should utilize the three pockets identified in the crystal structure of the PI4K IIα enzyme with MD59. The narrow deep pocket 1 might be effectively filled with a linear substituent. Significant space for modification is opened in pocket 2, which is formed mostly by lipophilic residues. The interaction of Asp346 with pocket 3 seems to be essential for adequate affinity of the ligand for the kinase and should be exploited preferably by ionic interaction. (c) MD59 docked into PI4K IIIβ. MD59 was docked into PI4K IIIβ in the same orientation as that in which it interacts with PI4K IIα. However, superposition with the ATP adenine ring reveals that it is rotated by 60° and that its hydroxyl group cannot form hydrogen bonds to any residue. The N-lobe of PI4K IIIβ is shown in orange and the C-lobe is shown in cyan. MD59 C atoms are coloured grey and C atoms of the ATP adenine ring are coloured green.

nucleotide is capable of binding to this pocket (Baumlova *et al.*, 2014); thus, we included ADP in the crystallization condition. To prevent ADP from competing with MD59, we added ADP at a low concentration (0.5 m*M*) while keeping the concentration of MD59 high (2 m*M*). The resulting crystals diffracted to 2.6 Å resolution (albeit with some anisotropy) and density for MD59 was clearly visible (Fig. 6*a*). The side chain of Asp346 has changed conformation to form hydrogen bonds to the hydroxyl group of MD59 (Fig. 6*a*, Supplementary Fig. S3*a*); notably in this conformation it would clash with the α-phosphate of ADP. To further confirm that the ligand density is not from the sterically similar ADP molecule, we built ADP instead of MD59 in the same conformation as reported by Zhou and coworkers (Supplementary Figs. S3*b* and S3*c*). Our structure clearly has no density for phosphates, which were well visible in previously reported structures of PI4K IIα (Baumlova *et al.*, 2014; Zhou *et al.*, 2014).

The structure revealed three pockets in the proximity of MD59 (numbered 1, 2 and 3 in Fig. 6*b*) that could be exploited for the design of highly selective and potent inhibitors of type II PI4Ks. Since pocket 1 appears to be narrow, a linear substituent such as acetylene may be suitable to attach to the adenine ring to appropriately fill this space. In addition, a large aromatic substituent either on the adenylyl or ribosyl ring could fill pocket 2 and a charged group (for example amidine or guanidine) attached to the ribosyl ring could fill pocket 3.

We have shown above that nucleoside scaffold-based inhibitors only inhibit the atypical type II PI4Ks (Fig. 5*b*). To understand why, we took advantage of the structure of PI4K IIIβ bound to ATP that we have recently solved (Mejdrova *et al.*, 2015). We have docked MD59 in the PI4K IIIβ in the same orientation that it has when bound to PI4K IIα (Fig. 6*c*). Docking revealed that the MD59 adenine ring would be rotated by 60° compared with the ATP adenine ring and thus unable to form the key hydrogen bonds to Glu572 and Lys564. The MD59 hydroxyl group that is important for inhibition of type II kinases also does not form any hydrogen bonds to the type III kinase. Previously, we have prepared highly selective inhibitors against PI4K IIIβ (Mejdrova *et al.*, 2015); we now show that inhibitors with a nucleoside scaffold only inhibit the atypical type II PI4Ks and are thus the perfect starting point for isoform-specific inhibitor design.

Structural analysis of the catalytic sites of PI4K IIα and PI4K IIβ (Fig. 4*b*) revealed only a few differences, implying that the design of an inhibitor discriminating between the IIα and IIβ isoenzymes would be rather difficult. One difference potentially useful for isoform-specific inhibitor design is the orientation of residue Ser127 of PI4K IIβ, which corresponds to Tyr131 in the PI4K IIα enzyme. Neither Ser127 nor Tyr131 contact ATP directly, but are in close proximity. A PI4K IIα-specific inhibitor must have a group that is capable of interaction with the aromatic ring of Tyr131, for example a small aromatic ring (π-stacking) or an –SH, –S*R* or positively charged group, whereas a PI4K IIβ-specific inhibitor must have a bulky non-aromatic group that would sterically interfere with Tyr131 but would be capable of hydrogen bonding to Ser127.

Taken together, our results provide a structural basis for the design of specific inhibitors of type II PI4Ks.

References

Adams, P. D. *et al.* (2010). *Acta Cryst.* D**66**, 213–221.
Altan-Bonnet, N. & Balla, T. (2012). *Trends Biochem. Sci.* **37**, 293–302.
Anglin, J. L., Deng, L., Yao, Y., Cai, G., Liu, Z., Jiang, H., Cheng, G., Chen, P., Dong, S. & Song, Y. (2012). *J. Med. Chem.* **55**, 8066–8074.
Balla, T. (1998). *Biochim. Biophys. Acta*, **1436**, 69–85.
Balla, T. (2013). *Physiol. Rev.* **93**, 1019–1137.
Balla, A., Tuymetova, G., Barshishat, M., Geiszt, M. & Balla, T. (2002). *J. Biol. Chem.* **277**, 20041–20050.
Barylko, B., Gerber, S. H., Binns, D. D., Grichine, N., Khvotchev, M., Südhof, T. C. & Albanesi, J. P. (2001). *J. Biol. Chem.* **276**, 7705–7708.
Baumlova, A., Chalupska, D., Różycki, B., Jovic, M., Wisniewski, E., Klima, M., Dubankova, A., Kloer, D. P., Nencka, R., Balla, T. & Boura, E. (2014). *EMBO Rep.* **15**, 1085–1092.
Berger, K. L., Cooper, J. D., Heaton, N. S., Yoon, R., Oakland, T. E., Jordan, T. X., Mateu, G., Grakoui, A. & Randall, G. (2009). *Proc. Natl Acad. Sci. USA*, **106**, 7577–7582.
Bianco, A., Reghellin, V., Donnici, L., Fenu, S., Alvarez, R., Baruffa, C., Peri, F., Pagani, M., Abrignani, S., Neddermann, P. & De Francesco, R. (2012). *PLoS Pathog.* **8**, e1002576.
Boura, E. & Hurley, J. H. (2012). *Proc. Natl Acad. Sci. USA*, **109**, 1901–1906.
Boura, E., Ivanov, V., Carlson, L. A., Mizuuchi, K. & Hurley, J. H. (2012). *J. Biol. Chem.* **287**, 28144–28151.
Boura, E., Rezabkova, L., Brynda, J., Obsilova, V. & Obsil, T. (2010). *Acta Cryst.* D**66**, 1351–1357.
Burgess, J., Del Bel, L. M., Ma, C.-I. J., Barylko, B., Polevoy, G., Rollins, J., Albanesi, J. P., Krämer, H. & Brill, J. A. (2012). *Development*, **139**, 3040–3050.
Burke, J. E., Inglis, A. J., Perisic, O., Masson, G. R., McLaughlin, S. H., Rutaganira, F., Shokat, K. M. & Williams, R. L. (2014). *Science*, **344**, 1035–1038.
Craige, B., Salazar, G. & Faundez, V. (2008). *Mol. Biol. Cell*, **19**, 1415–1426.
Debreczeni, J. É. & Emsley, P. (2012). *Acta Cryst.* D**68**, 425–430.
Dejmek, M. *et al.* (2015). *Bioorg. Med. Chem.* **23**, 184–191.
Greninger, A. L., Knudsen, G. M., Betegon, M., Burlingame, A. L. & DeRisi, J. L. (2012). *J. Virol.* **86**, 3605–3616.
Hurley, J. H., Boura, E., Carlson, L. A. & Różycki, B. (2010). *Cell*, **143**, 875–887.
Jović, M., Kean, M. J., Dubankova, A., Boura, E., Gingras, A. C., Brill, J. A. & Balla, T. (2014). *J. Cell Sci.* **127**, 3745–3756.
Jović, M., Kean, M. J., Szentpetery, Z., Polevoy, G., Gingras, A. C., Brill, J. A. & Balla, T. (2012). *Mol. Biol. Cell*, **23**, 1533–1545.

Jung, G., Barylko, B., Lu, D., Shu, H., Yin, H. & Albanesi, J. P. (2011). *J. Biol. Chem.* **286**, 12775–12784.

Jung, G., Wang, J., Wlodarski, P., Barylko, B., Binns, D. D., Shu, H., Yin, H. L. & Albanesi, J. P. (2008). *Biochem. J.* **409**, 501–509.

Kabsch, W. (2010). *Acta Cryst.* D**66**, 125–132.

Karplus, P. A. & Diederichs, K. (2012). *Science*, **336**, 1030–1033.

Kim, D. J. *et al.* (2010). *Proc. Natl Acad. Sci. USA*, **107**, 21418–21423.

Krug, M., Weiss, M. S., Heinemann, U. & Mueller, U. (2012). *J. Appl. Cryst.* **45**, 568–572.

McCoy, A. J., Grosse-Kunstleve, R. W., Adams, P. D., Winn, M. D., Storoni, L. C. & Read, R. J. (2007). *J. Appl. Cryst.* **40**, 658–674.

Mejdrova, I. *et al.* (2015). *J. Med. Chem.* **58**, 3767–3793.

Minogue, S., Waugh, M. G., De Matteis, M. A., Stephens, D. J., Berditchevski, F. & Hsuan, J. J. (2006). *J. Cell Sci.* **119**, 571–581.

Moorhead, A. M., Jung, J.-Y., Smirnov, A., Kaufer, S. & Scidmore, M. A. (2010). *Infect. Immun.* **78**, 1990–2007.

Nemecek, D., Boura, E., Wu, W., Cheng, N., Plevka, P., Qiao, J., Mindich, L., Heymann, J. B., Hurley, J. H. & Steven, A. C. (2013). *Structure*, **21**, 1374–1383.

Qin, Y., Li, L., Pan, W. & Wu, D. (2009). *J. Biol. Chem.* **284**, 22544–22548.

Rosenbaum, D. M., Cherezov, V., Hanson, M. A., Rasmussen, S. G. F., Thian, F. S., Kobilka, T. S., Choi, H.-J., Yao, X.-J., Weis, W. I., Stevens, R. C. & Kobilka, B. K. (2007). *Science*, **318**, 1266–1273.

Różycki, B. & Boura, E. (2014). *J. Phys. Condens. Matter*, **26**, 463103.

Różycki, B., Boura, E., Hurley, J. H. & Hummer, G. (2012). *PLoS Comput. Biol.* **8**, e1002736.

Sasaki, J., Ishikawa, K., Arita, M. & Taniguchi, K. (2012). *EMBO J.* **31**, 754–766.

Schaar, H. M. van der *et al.* (2013). *Antimicrob. Agents Chemother.* **57**, 4971–4981.

Tai, A. W., Bojjireddy, N. & Balla, T. (2011). *Anal. Biochem.* **417**, 97–102.

Tan, J. & Brill, J. A. (2014). *Crit. Rev. Biochem. Mol. Biol.* **49**, 33–58.

Wang, K., Yang, Z., Liu, X., Mao, K., Nair, U. & Klionsky, D. J. (2012). *J. Biol. Chem.* **287**, 37964–37972.

Waugh, M. G. (2015). *Biochim. Biophys. Acta*, **1851**, 1066–1082.

Weber, S. S., Ragaz, C., Reus, K., Nyfeler, Y. & Hilbi, H. (2006). *PLoS Pathog.* **2**, e46.

Wei, Y. J., Sun, H. Q., Yamamoto, M., Wlodarski, P., Kunii, K., Martinez, M., Barylko, B., Albanesi, J. P. & Yin, H. L. (2002). *J. Biol. Chem.* **277**, 46586–46593.

Winn, M. D. *et al.* (2011). *Acta Cryst.* D**67**, 235–242.

Wu, X., Chi, R. J., Baskin, J. M., Lucast, L., Burd, C. G., De Camilli, P. & Reinisch, K. M. (2014). *Dev. Cell*, **28**, 19–29.

Zhou, Q., Li, J., Yu, H., Zhai, Y., Gao, Z., Liu, Y., Pang, X., Zhang, L., Schulten, K., Sun, F. & Chen, C. (2014). *Nature Commun.* **5**, 3552.

Zou, Y., Weis, W. I. & Kobilka, B. K. (2012). *PLoS One*, **7**, e46039.